

Advanced methods for loss-of-flow accident precursors identification in a superconducting magnet cryogenic cooling circuit

Original

Advanced methods for loss-of-flow accident precursors identification in a superconducting magnet cryogenic cooling circuit / Destino, V., Bonifetto, R., Pedroni, N., Savoldi, L., Di Maio, F., Zio, E., Zio, E.. - ELETTRONICO. - (2020), pp. 2303-2310. (30th European Safety and Reliability Conference, ESREL 2020 and 15th Probabilistic Safety Assessment and Management Conference, PSAM 2020 ita 2020).

Availability:

This version is available at: 11583/2946452 since: 2021-12-18T16:00:47Z

Publisher:

Research Publishing Services

Published

DOI:

Terms of use:

This article is made available under terms and conditions as specified in the corresponding bibliographic description in the repository

Publisher copyright

(Article begins on next page)

On the impact of the orifice shape in acoustic liner attenuation under turbulent grazing flow

Angelo Paduano* and Francesco Scarano[†]
Politecnico di Torino, Corso Duca degli Abruzzi 24, 10122, Torino, Italy

Damiano Casalino[‡]
Delft University of Technology, Kluyverweg 1, 2629HS, Delft

Julio A. Cordioli[§]
Federal University of Santa Catarina, Florianópolis - SC, 88040-900, Brazil

Francesco Avallone[¶]
Politecnico di Torino, Corso Duca degli Abruzzi 24, 10122, Torino, Italy

This work investigates the influence of orifice-edge geometry on the aeroacoustic performance of perforated acoustic liners exposed to turbulent grazing flow. Two liner geometries are compared. They differ only for the shape of the facesheet orifices. One has sharp edge orifices, while the other chamfered edge orifices. The internal diameter, the facesheet thickness and the cavity depth is the same. High-fidelity lattice-Boltzmann very-large-eddy simulations are performed and compared with experimental measurements to assess both the acoustic response and the underlying flow physics. Impedance reduction reveals that the sharp-edged liner exhibits up to 50% higher acoustic resistance over the investigated frequency range, whereas the reactance remains broadly similar, apart from a shift in resonance frequency from approximately 1.7 to 1.9 kHz. Flow-field analysis indicates that the chamfered geometry promotes stronger momentum exchange and weaker shear layers strength above the orifices, effectively behaving as a more permeable surface. These findings show that small manufacturing-scale variations in orifice-edge shape can significantly alter both the aerodynamic development and the acoustic attenuation of liners under grazing flow, highlighting the need to account for edge geometry in liner design and predictive modeling.

Symbols and Acronyms

Z	=	Impedance
θ	=	Resistance
χ	=	Reactance
L	=	Length of the liner
l	=	Width of each square cavity
τ	=	Face-sheet thickness
ω_p	=	Partition wall thickness
d	=	Orifice diameter
λ	=	Cavity depth
f	=	Frequency
SPL	=	Sound Pressure Level

*PhD student, Department of Mechanical and Aerospace Engineering, angelo.paduano@polito.it.

[†]Post-Doc, Department of Mechanical and Aerospace Engineering, francesco.scarano@polito.it.

[‡]Full Professor, Department of Flow Physics and Technology, d.casalino@tudelft.nl, AIAA member.

[§]Associate Professor, Department of Mechanical Engineering, julio.cordioli@ufsc.br, AIAA member.

[¶]Full Professor, Department of Mechanical and Aerospace Engineering, francesco.avallone@polito.it, AIAA member.

- M = Mach number
- C_f = Skin-friction coefficient
- $\hat{\cdot}$ = Acoustic-induced quantities

I. Introduction

ACOUSTIC liners are essential for mitigating both tonal and broadband fan noise in modern turbofan engines [1, 2], a requirement driven by increasingly stringent international noise standards and public demand for quieter air travel. Traditional liners combine a perforated facesheet, a honeycomb core, and a rigid backing plate, forming a resonant system designed primarily to target the fan blade passage frequency [2].

The operational principle relies on the classical Helmholtz resonator mechanism, wherein the combined mass of the air in the orifices and the compliance of the underlying cavity create a resonant acoustic absorber [3]. In the absence of grazing flow, acoustic energy dissipation mainly occurs through viscous and thermal losses within the necks, as well as vortex shedding at the perforation edges [4–7]. A key parameter used to characterise liner attenuation is the acoustic impedance $Z(\omega)$, defined in the complex domain as the ratio of the acoustic pressure \hat{p} (such that $p(\mathbf{x}, t) = \Re(\hat{p} e^{i\omega t})$), and the acoustic particle velocity \hat{v} . The real part of Z is termed the resistance (θ), while the imaginary part is the reactance (χ). Acoustic impedance is a function of frequency, sound pressure level (SPL), and it depends on the detailed geometry of the liner, including orifice shape, diameter, facesheet thickness and cavity depth [8]. Both experimental and numerical investigations have demonstrated that variations in these geometric features modify the liner impedance and the resulting acoustic waves attenuation [9–11]. Advances in acoustic liner design have focused extensively on optimising orifice shape and distribution to increase broadband absorption, particularly under high SPL representative of engine conditions [2]. While most prior studies address liners in quiescent or uniform flow conditions, the presence of a turbulent grazing flow introduces additional complexity. Grazing flow affects the effective acoustic impedance of liners by causing a blockage effect over the orifice, thus changing the energy dissipation and the acoustic response of the liner [12, 13].

Recently, Paduano et al. [13] demonstrated through high-fidelity simulations that an acoustic liner subjected to acoustic waves modifies the mean flow profile above cavity orifices and consequently affects the local acoustic fields within. These flow modifications are mainly caused by the presence of orifices and by the interaction between acoustic wave propagation and the turbulent flow, spatially influencing liner absorption characteristics. The spatial development of the turbulent grazing flow and acoustic wave directionality further complicates this interaction [13]. However, the impact of the orifice geometry on the turbulent grazing flow and on the liner performance remains only partially understood. In particular, there is limited insight into how small variations in the orifice edge profile affect the coupled hydrodynamic and acoustic fields. This issue is of practical importance, as such variations are often comparable to those introduced by manufacturing tolerances, deburring processes, or surface finishing techniques. Geometric details that are typically considered negligible may in fact influence the effective impedance, the shear-layer development above the perforations, and the acoustic attenuation [14].

The present work addresses this gap by systematically investigating the influence of orifice edge geometry on both the aeroacoustic performance and the turbulent flow development of liners under realistic grazing-flow conditions. Two configurations are considered, differing only in the orifice edge shape—sharp-edged and chamfered—while retaining the same internal diameter, facesheet thickness, and cavity depth. This controlled comparison makes it possible to isolate the effect of manufacturing-scale geometric variations and to relate them directly to both the acoustic response and the underlying flow topology. By combining high-fidelity simulations with experimental results, the study aims to improve the physical understanding of the mechanisms governing liner performance and to provide guidance for the design of more effective noise-reduction devices.

The remainder of the paper is organised as follows. Section II describes the numerical methodology, Section III presents the impedance reduction approach, Section IV discusses the results, and Section V summarises the main conclusions.

II. Computational method

A. Flow solver

The commercial solver 3DS Simulia PowerFLOW[®] (version 6) is employed. It is based on the Lattice Boltzmann Method (LBM), which describes the fluid at a mesoscopic level through particle distribution functions whose moments recover macroscopic quantities such as density and velocity [15].

In LBM, the evolution of the particle distribution function g follows a discretised form of the Boltzmann equation, where particle streaming and collisions are solved on a Cartesian lattice. The Bhatnagar–Gross–Krook (BGK) approximation is used for the collision operator:

$$\Omega(g) = -\frac{1}{\tau}(g - g^{eq}), \quad (1)$$

where τ is the relaxation time and g^{eq} is the equilibrium distribution. The D3Q19 lattice scheme is adopted [16]. Macroscopic quantities are obtained as moments of the distribution functions:

$$\rho = \sum_i g_i, \quad \rho \mathbf{u} = \sum_i \xi_i g_i. \quad (2)$$

Turbulence is modelled using a Very Large Eddy Simulation (VLES) approach, in which only the largest scales are resolved. Sub-grid effects are accounted for through a modified relaxation time:

$$\tau_{\text{eff}} = \tau + C_\mu \frac{k^2/\epsilon}{(1 + \eta^2)^{1/2}}, \quad (3)$$

based on the RNG k - ϵ model [17]. In this framework, the turbulence model acts by adjusting the local relaxation properties of the kinetic equation, rather than directly providing Reynolds stresses as in RANS formulations.

Near-wall effects are treated using a pressure-gradient-enhanced wall model (PGE-WM) [18], which modifies the classical law of the wall:

$$u^+ = \frac{1}{\kappa} \ln \left(\frac{y^+}{A} \right) + B, \quad (4)$$

where A accounts for the local pressure gradient. This correction captures the modification of the velocity profile due to adverse or favourable pressure gradients.

B. Computational Setup

The computational domain is shown in Figure 1, with coordinate axes defined as x (streamwise), y (wall-normal), and z (spanwise). Velocity components are denoted as U, V, W for time-averaged and u, v, w for instantaneous velocities, with fluctuations defined as $u' = u - U$, and similarly for v' and w' .

The acoustic liner is positioned along the centre of the top wall of a rectangular duct. Two liner geometries are considered: one with sharp-edged orifices and one with chamfered edges, as illustrated in Figure 1 (c, d). The two configurations differ only in the orifice edge profile, which results in different effective diameters at the grazing-flow interface, equal to $d = 1.00$ mm and $d = 1.20$ mm, respectively, while maintaining the same internal diameter $D = 1.00$ mm. These variations are representative of realistic manufacturing tolerances, such as those arising from additive manufacturing processes. In particular, while the internal diameter is preserved, modifications to the orifice edge shape alter the effective opening perceived by the grazing flow. As a result, although the nominal porosity based on the internal diameter remains constant at 4.00%, the porosity perceived by the grazing flow is higher for the chamfered configuration, reaching approximately 5.86%. Apart from these differences in edge shaping, all other geometric parameters are identical. Each cavity measures $l = 12.46$ mm in width and $\lambda = 38.10$ mm in depth. Each cavity contains eight orifices (see Figure 1e), partition walls of thickness $w_p = 2.53$ mm, and a facesheet of thickness $\tau = 0.64$ mm. The channel cross-section has a height $H = 40.00$ mm and a width of $l + w_p$.

Upstream of the liner, a zig-zag trip, 0.24 mm in height and 2.00 mm in length, was installed on both the top and bottom walls at $x = -1599.00$ mm to replicate the experimentally measured velocity profile [19]. To prevent acoustic reflections at the duct outlet, sponge regions were introduced in which viscosity was progressively increased by a factor of 100, as shown in Figure 1 (a). All duct walls are adiabatic. At the inlet, a uniform velocity corresponding to Mach 0.3 was imposed, leading to a centerline velocity of $U_0 = 110$ m/s in the lined section. A pressure boundary condition was set at the outlet.

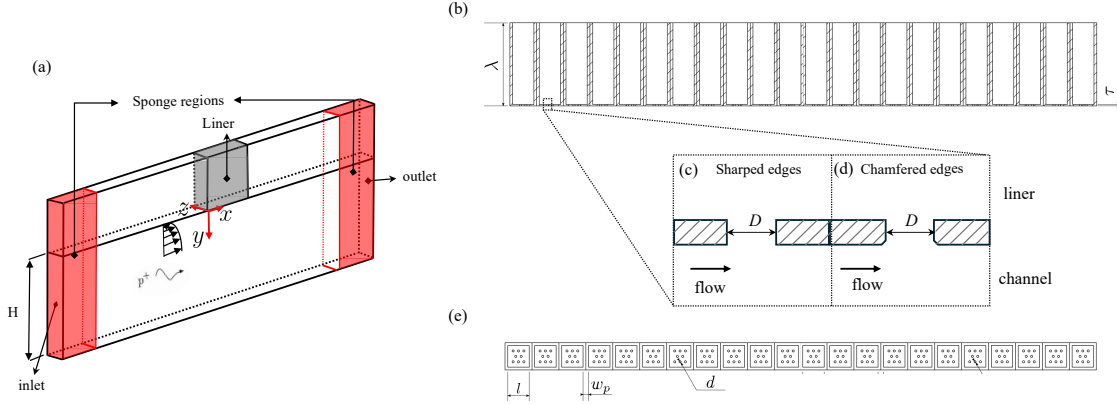


Fig. 1 Sketch of the numerical setup (a) 3D geometry, (b) 2D cross-plane of the acoustic liner, (c, d) sketch of the edge shapes of the two geometries tested, (e) facesheet detail of the liners.

The present simulations have been compared with experiments conducted on the same liner geometries at the Federal University of Santa Catarina (UFSC) and will be presented in a companion paper at this conference. The computational domain replicates the main features of the UFSC Liner Test Rig used in the experiments. The numerical model employs a single row of 22 cavities, compared to the experimental 8×18 cavity layout, but maintains an identical orifice count per cavity and equivalent porosity. Periodic boundary conditions are applied laterally, in contrast to the experimental rectangular duct ($100 \times 40 \text{ mm}^2$), a modelling choice previously shown to have negligible impact on the predicted acoustic response [13, 20].

C. Mesh and simulation strategy

A Variable Resolution (VR) mesh was utilised, symmetric about the channel centerline. The finest grid level (VR=7) covered the facesheet, orifices, and portions of the cavity backing, employing a minimum cell size of $\Delta x = \Delta y = \Delta z = 0.02d$ —corresponding to approximately 50 cells across the orifice diameter. This mesh density was selected based on prior sensitivity studies, which demonstrated that further refinement yields negligible impact on the simulated results [13].

Simulations were executed in two phases. First, flow-only calculations were performed under grazing flow conditions until statistical convergence was reached. The convergence was assessed in terms of the mean velocity profiles and second-order statistics at the beginning of the lined section. Subsequently, plane acoustic waves of prescribed frequency and amplitude were superimposed on instantaneous flow fields using the *OptydB* toolkit [21]. In the acoustic simulation, the pressure field was sampled over a time window sufficient to ensure converged spectral amplitudes at the forcing frequency.

This two-step approach explicitly accounts for the interaction between acoustic waves and unsteady turbulence [13, 22], unlike approaches where the acoustic perturbation is linearised around the mean flow solution [12, 23]. Moreover, this methodology captures the inherently nonlinear response of the liner when exposed to a grazing acoustic wave at 145 dB, since the interaction between the unsteady turbulence and the imposed acoustic field is directly resolved rather than assumed linear a priori. The main drawback of this approach is the requirement for the computational domain to be sufficiently long to accommodate at least ten acoustic wavelengths of the lowest frequency of interest. However, this method significantly reduces computational costs when evaluating multiple configurations, making it an efficient choice for parametric studies. Moreover, it has already been successfully applied and validated in previous works [13].

In total, twenty-four distinct simulations were conducted, varying wave frequency, SPL, and the location of the acoustic source (upstream or downstream of the liners) to provide a comprehensive characterisation of liner performance. For conciseness, the results presented herein focus on cases corresponding to acoustic waves with SPL equal to 130 and 145 dB, three representative frequencies, and an upstream source location.

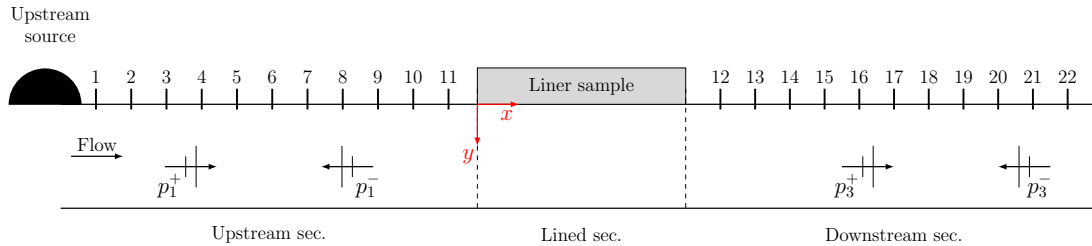


Fig. 2 Representation of the acoustic field in the mode matching method and schematic view of the test rig. Adapted from [26].

III. Impedance Eduction technique

1. Mode Matching method

The Mode Matching (MM) technique is an inverse impedance eduction method in which the liner impedance is obtained by minimising the discrepancy between the measured acoustic field and an analytical solution. The method was introduced by Elnady and Bodén [24] and later validated by Elnady et al. [25].

The MM approach requires pressure measurements upstream and downstream of the liner, as sketched in Figure 2. The acoustic field in the hard-wall sections is represented as a modal expansion, with waves propagating both upstream and downstream. In the present configuration, only plane waves propagate in these sections, since the investigated frequencies are below the first cut-on frequency. The acoustic sponge layers prevent reflections from the duct termination; therefore, only the incident and liner-scattered waves are retained in the reconstruction of the acoustic field. Viscothermal losses are included through a correction of the plane-wave axial wavenumber.

The modal amplitudes are obtained from the pressure measurements by solving an over-determined least-squares system using eleven microphones in each hard-wall section. These amplitudes are then used as input to the MM model. Starting from an initial impedance estimate provided by the semi-empirical model of Yu et al. [27], the liner impedance is iteratively determined using the Levenberg–Marquardt algorithm [28, 29]. The converged value is retained as the educed liner impedance.

2. In-situ technique

The in-situ technique, also referred to as the Dean’s method, was first proposed by Dean [30]. It provides a point-wise estimate of the liner impedance from unsteady pressure measurements at the facesheet and at the cavity backplate. The method assumes that the acoustic wavelength is much larger than the cavity width, that the liner behaves locally reactively, and that the acoustic waves entering the cavity are reflected at the rigid backplate.

Under these assumptions, the pressure field inside the cavity is described as a standing wave, and the impedance is obtained from the transfer function between the facesheet and backplate pressure signals. This technique is widely used for liners under grazing-flow conditions [31, 32]. In contrast to impedance eduction methods, it does not require a flow-based boundary condition to account for near-wall acoustic–flow interactions. However, its sensitivity to the probe location has been previously reported [13]. Since the simulations provide pressure data over the entire liner surface, the minimum, maximum, and mean impedance values across the cavities are also extracted.

IV. Results and Discussion

A. Acoustic behaviour

The comparison between the two geometries begins with the streamwise distribution of the SPL in the channel for the two facesheet geometries shown in Figure 3. Each profile is normalised by the incident level, to isolate the relative attenuation across the lined section. At the lowest frequency considered, $f = 800$ Hz (Figure 3(a)), both configurations display weak attenuation. This limited decay is attributed to the large acoustic wavelength compared with the liner length, which restricts spatial attenuation within the treated region. As the frequency increases to 1400 Hz (Figure 3(b)) and 2000 Hz (Figure 3(c)) the SPL decreases more rapidly. The chamfered liner exhibits the larger decay at all frequencies, providing nearly 4 dB of additional attenuation at 2000 Hz compared with the sharp-edged geometry. This

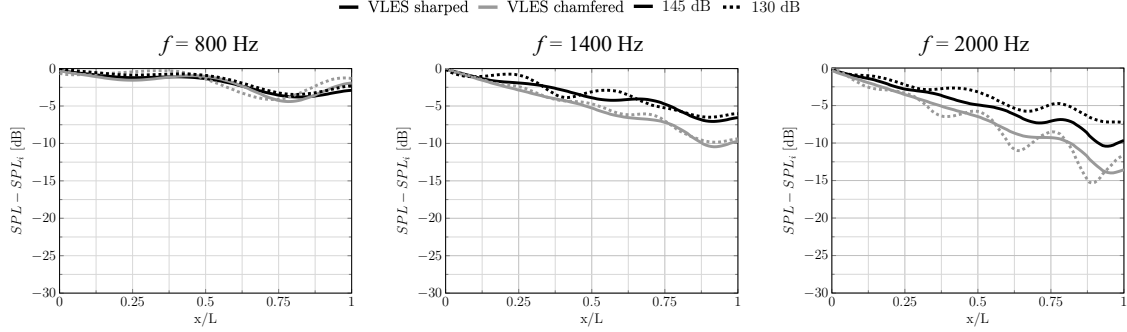


Fig. 3 Streamwise SPL decay over the liner for both facesheet geometries. (a) $f = 800$ Hz, (b) $f = 1400$ Hz, and (c) $f = 2000$ Hz. The results are normalised by the incident value, $M = 0.3$, upstream source.

trend persists across all tested SPL levels, including the lower SPL case (130 dB).

1. Educated impedance

To further quantify the effect of the orifice edge profile on the acoustic properties of the liner, Figure 4 compares the resistance and reactance obtained using the MM technique for both liner geometries at two SPL levels, 130 dB and 145 dB. Numerical results, experimental measurements, and predictions from the semi-empirical model of Yu *et al.* [27] are shown for reference.

In all cases, the resistance exhibits a weak dependence on frequency, while the reactance increases, in agreement with trends reported in the literature [19, 33]. The close agreement between numerical and experimental results confirms the ability of the numerical framework to accurately reproduce the frequency-dependent impedance behaviour.

The semi-empirical model, in its original formulation, shows no sensitivity to changes in the orifice edge geometry, as it does not explicitly account for edge-shape effects [27]. To approximate this effect, the model has been applied using two different porosity values corresponding to the effective opening perceived by the grazing flow, namely $\sigma = 4.0\%$ for the sharp-edged configuration and $\sigma = 5.86\%$ for the chamfered one, despite the identical internal orifice diameter in both cases.

For both geometries, the resistance and reactance exhibit only a mild dependence on SPL, consistent with previous studies [13, 34]. However, a clear and systematic difference is observed between the two configurations: the sharp-edged geometry consistently exhibits higher resistance across all frequencies and SPLs. In particular, the chamfered configuration yields approximately 40% lower resistance than the sharp-edged one at 800 Hz, with the difference increasing to about 50% at 1400 and 2000 Hz.

This reduction in resistance is consistent with a larger effective opening exposed to the grazing flow and with the weaker shear-layer intensity observed in the flow-field analysis. In contrast, the reactance remains relatively similar between the two geometries over most of the frequency range, as expected since both configurations share the same cavity depth [8]. However, a shift in resonance frequency is observed, from approximately 1.7 kHz for the sharp-edged geometry to 1.9 kHz for the chamfered one. This shift can be attributed to a change in the effective acoustic mass near the orifice opening, which modifies the end correction [3].

These results indicate that modifications of the orifice edge shape affect both the resistive and reactive components of the impedance in a way that is analogous to a change in porosity, even though the internal orifice diameter remains unchanged. This behaviour is further illustrated in Figure 5, which reports the ratio of resistance and reactance between the two geometries for the case at 145 dB. Predictions from the semi-empirical model are also included using the adjusted porosity values described above.

With this correction, the semi-empirical model predicts a resistance ratio between the two geometries that is in good agreement with both numerical and experimental results, indicating that the dominant effect of edge modification on the resistive component can be captured through an effective change in porosity. In contrast, the reactance ratio remains close to unity over most of the frequency range, except in the interval between 1700 and 2000 Hz, where differences in resonance frequency between the two geometries produce an oscillatory behaviour. Although the model reproduces the general trend of the reactance ratio, it exhibits a systematic shift towards lower frequencies compared to the reference data.

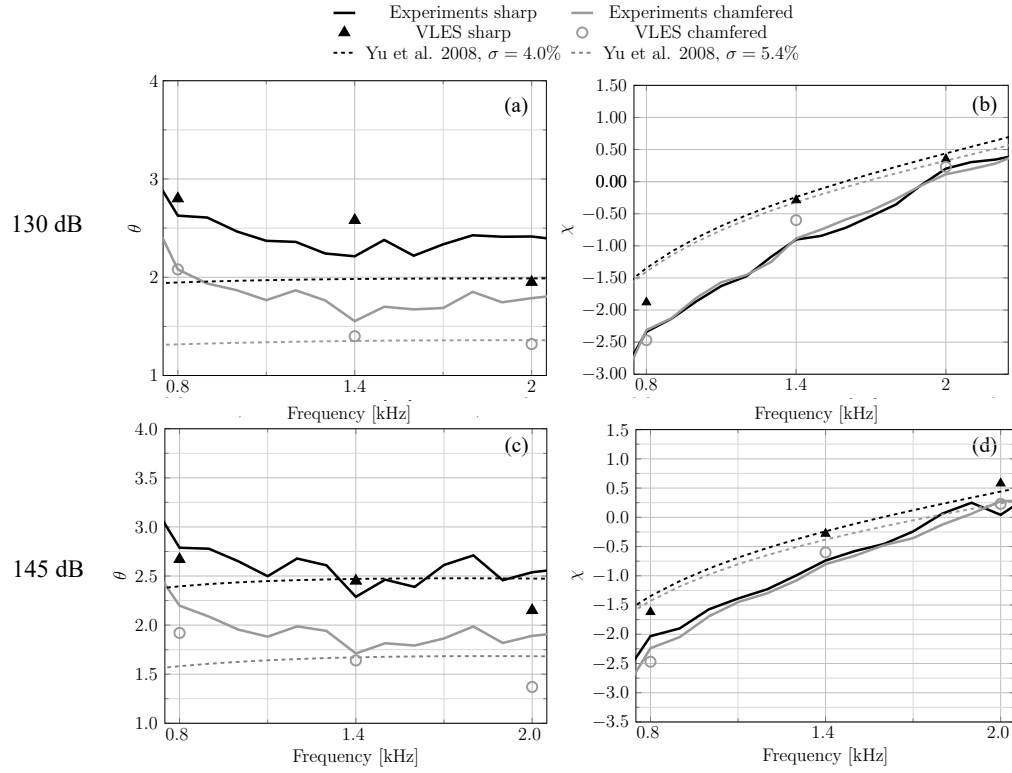


Fig. 4 Resistance and reactance obtained from numerical simulations, experiments, and the semi-empirical model proposed by Yu et al. [27]. (a)–(b) SPL = 130 dB; (c)–(d) SPL = 145 dB, $M = 0.3$, upstream source.

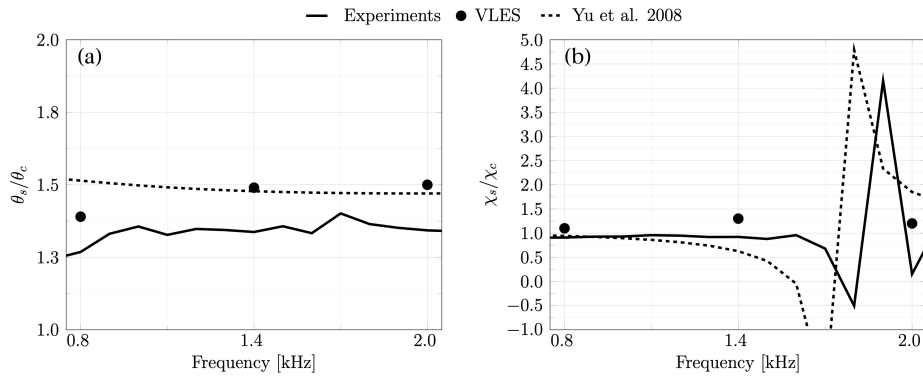


Fig. 5 Ratio of resistance (a) and reactance (b) between sharp-edged and chamfered geometries for SPL = 145 dB, $M = 0.3$, upstream acoustic source.

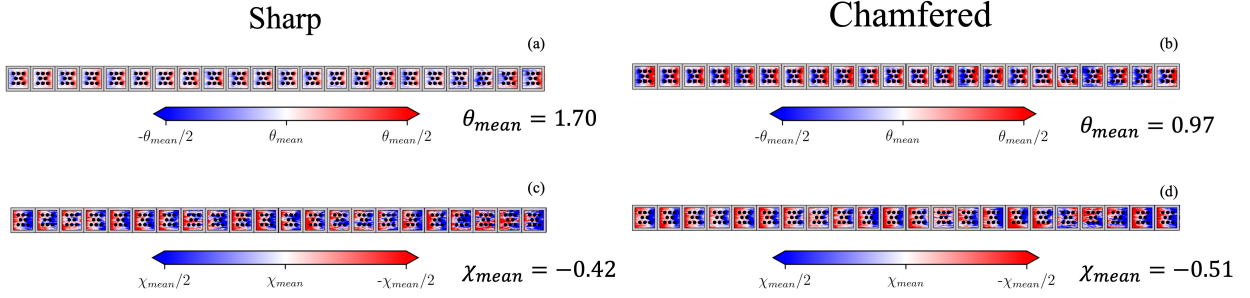


Fig. 6 In-situ impedance distribution at $M = 0.3$, $f = 1400$ Hz, and $\text{SPL} = 130$ dB. (a)–(b) Resistance and (c)–(d) reactance for sharp-edged (left) and chamfered (right) geometries.

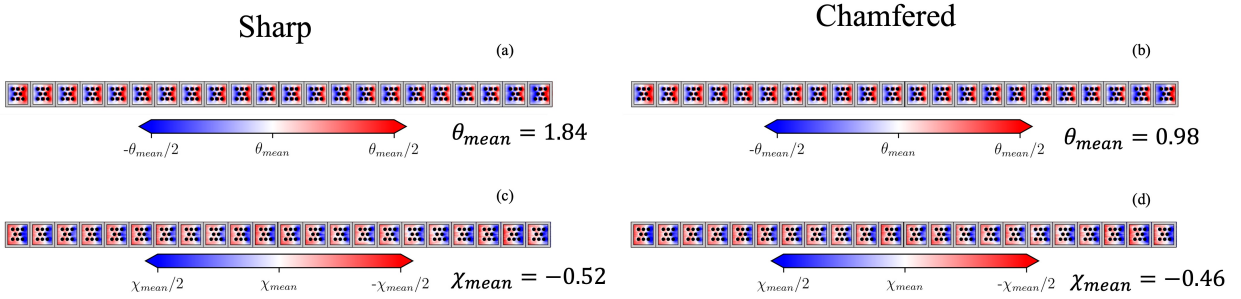


Fig. 7 In-situ impedance distribution at $M = 0.3$, $f = 1400$ Hz, and $\text{SPL} = 145$ dB. (a)–(b) Resistance and (c)–(d) reactance for sharp-edged (left) and chamfered (right) geometries.

This discrepancy highlights that porosity adjustments alone are not sufficient to fully capture the frequency-dependent behaviour of the impedance. In particular, the reactive component is also governed by geometry-dependent end effects and by the local flow–acoustic interaction at the orifice, which are not accounted for in the semi-empirical formulation.

This discrepancy highlights that modifying the surface porosity alone is not sufficient to fully capture the frequency-dependent behaviour of the impedance. In particular, the edge shape also affects the acoustic end correction and the local flow–acoustic interaction at the orifice entrance, which influence the effective oscillating mass of the fluid and, consequently, the resonance characteristics [3]. Therefore, while porosity adjustments can account for first-order changes in resistance, a more complete description of the impedance requires incorporating the detailed geometry and the associated near-orifice flow dynamics.

2. Local impedance distribution

The impedance maps obtained using the in-situ technique [30] are displayed in Figures 6 and 7. For each cavity, the impedance was determined from the pressure at the facesheet and the backplate to resolve spatial variations in both resistance and reactance. Reported mean values (θ_{mean} , χ_{mean}) correspond to the average across the entire facesheet.

The in-situ impedance maps confirm the global trends identified by the MM technique, namely a substantially lower mean resistance for the chamfered configuration, and a weak dependence of impedance on SPL. At 145 dB (Figure 6), the sharp-edged liner shows a mean resistance approximately twice that of the chamfered configuration ($\theta_{\text{mean}} \approx 1.84$ vs. 0.98). The mean reactance, on the other hand, differs only slightly between the two geometries ($\chi_{\text{mean}} \approx -0.52$ and -0.46). The same trends are observed at 130 dB, consistent with the MM results reported in Figure 4.

Beyond these global values, the in-situ maps reveal a distinct spatial organisation within each cavity. In particular, the resistance exhibits a periodic increase in the streamwise direction, with lower values near the upstream orifice and higher values toward the downstream side of each cavity. A similar, although less pronounced, pattern is also observed for the reactance. This behaviour might be caused by the local surface SPL, which depends on the local amplitude of the acoustic wave and the surface pressure fluctuations altered by the presence of the orifices [13], as it will be described later. This result explain the high sensitivity of Dean’s method to the facesheet probe location.

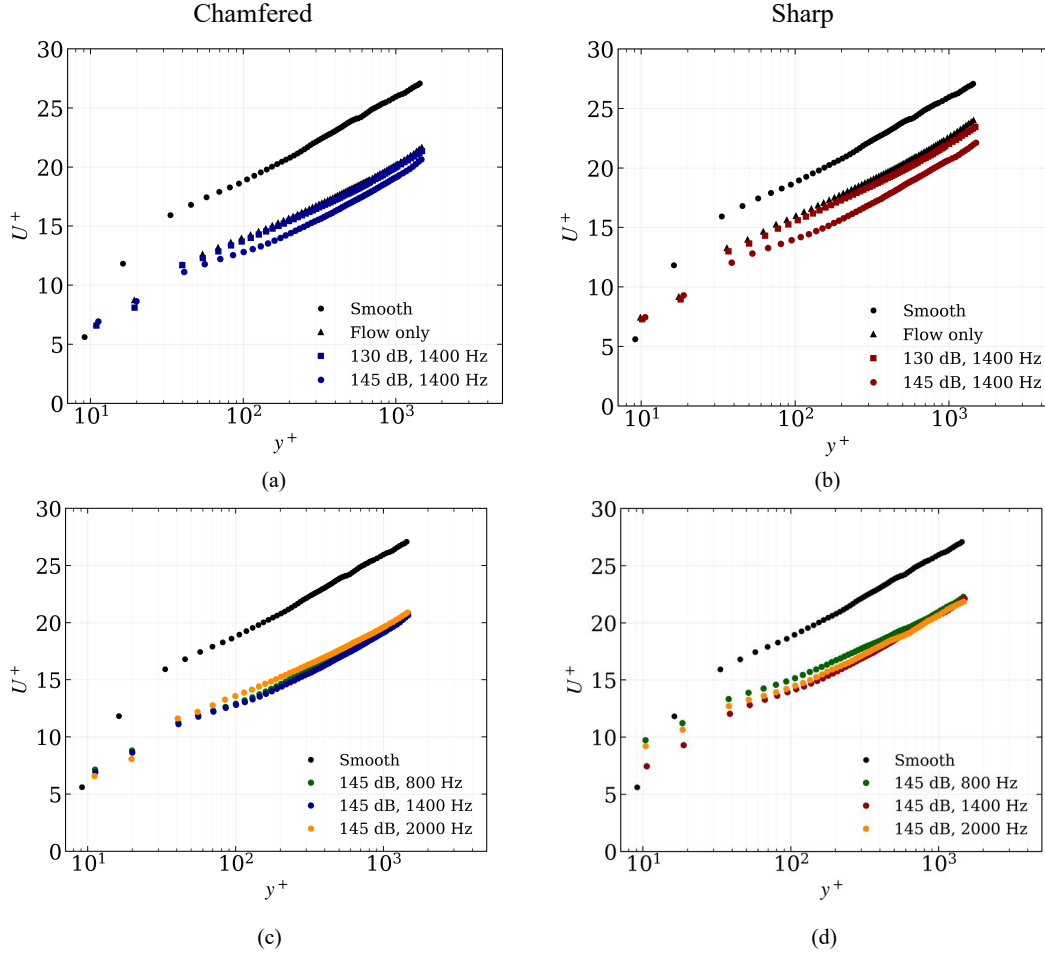


Fig. 8 Mean streamwise velocity in wall units (U^+) for the two facesheet geometries changing the SPL value ($SPL = 130, 145$ dB (a, b) at $f = 1400$ Hz) and changing frequency at $SPL = 145$ dB (c, d). All cases share the same Mach number equal to 0.3.

B. Flow field over the liner

The variation in acoustic response indicates that the grazing flow interacts differently with the two facesheet geometries, despite identical internal orifice diameter and cavity parameters. To better understand these differences, the mean and fluctuating velocity fields are analysed.

Figure 8(a) shows the mean streamwise velocity profiles in wall units at the downstream end of the liner. These results are compared with a smooth-wall reference case with the same channel geometry and bulk Mach number [13]. The friction velocity is estimated from the streamwise pressure gradient obtained between the inlet and outlet of the liner section. The wall shear stress is computed as $\tau_w = -h(dp/dx)$, and the corresponding skin-friction coefficient is given by $C_f = \tau_w / (1/2\rho U_b^2)$, where U_b is the bulk velocity.

Both configurations exhibit a downward shift of the logarithmic region compared to the smooth-wall case, indicating an increase in near-wall momentum deficit. This shift increases with SPL and shows only a weak dependence on frequency. Notably, the chamfered configuration consistently produces a larger downward shift than the sharp-edged one. Similar behaviour has been reported for liners with different porosities [35], where increased surface permeability leads to a stronger impact on the grazing flow. To further quantify this effect, the streamwise development of the boundary layer is analysed by comparing the flow-only case with the acoustically forced case ($SPL = 145$ dB, $f = 1400$ Hz), as shown in Figure 9.

In the absence of acoustic forcing, both geometries exhibit a rapid increase in boundary-layer thickness δ over the initial portion of the liner, followed by a gradual approach to a plateau downstream. At the liner exit, the chamfered

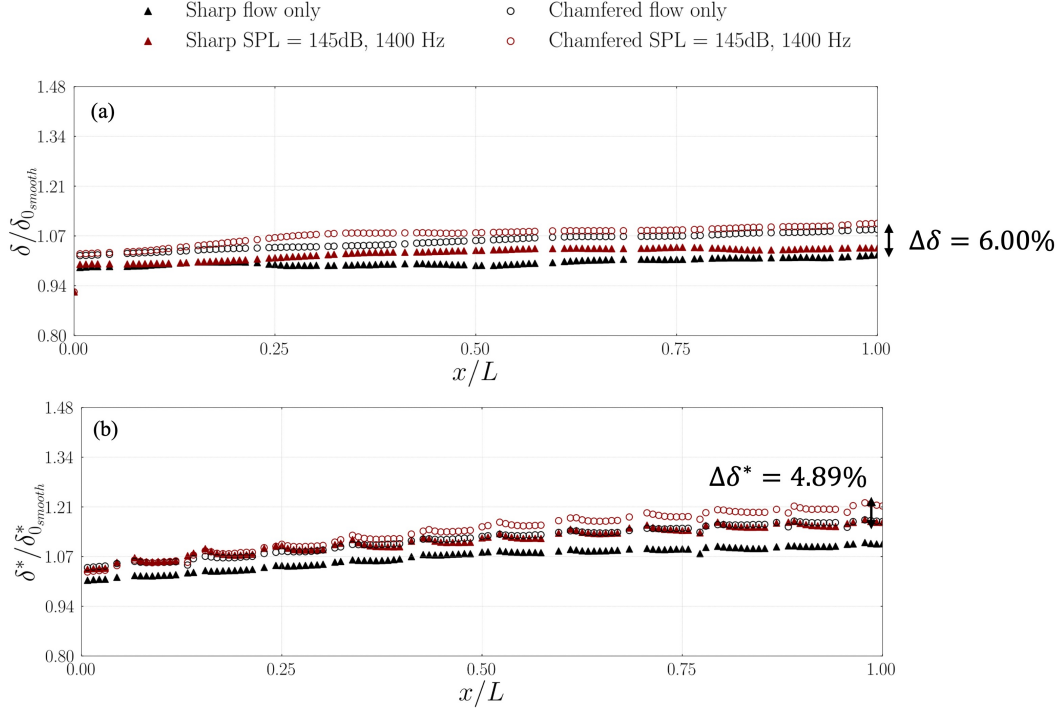


Fig. 9 Streamwise evolution of the boundary-layer thickness δ and displacement thickness δ^* , normalised by upstream smooth-wall values. Cases without acoustic forcing are compared with cases at $SPL = 145$ dB and $f = 1400$ Hz, with an upstream acoustic source. All cases correspond to a Mach number of $M = 0.3$.

configuration shows a boundary-layer thickness approximately 6% larger than that of the sharp-edged case.

When acoustic forcing is introduced, an overall increase in boundary-layer growth is observed for both geometries. However, the relative difference between the two configurations remains essentially unchanged.

A similar behaviour is observed for the displacement thickness δ^* , which increases along the streamwise direction and is further enhanced under acoustic forcing. The chamfered geometry consistently exhibits a larger displacement thickness, with an increase of approximately 5% compared to the sharp-edged case.

These results indicate that the chamfered geometry promotes a stronger exchange of momentum between the cavity flow and the outer stream, which increases when the acoustic forcing is present, leading to enhanced boundary-layer displacement thickness growth. This increased flow mixing suggests a higher effective permeability of the facesheet, despite identical nominal geometric parameters [36, 37].

1. Near-wall organisation and shear-layer dynamics

To explain the physical mechanism underlying the enhanced near-wall velocity deficit, contours of the standard deviation of the streamwise and wall-normal velocity components for the sixth cavity are shown in Figure 10. These fields provide insight into the unsteady flow structures developing within and above the liner orifices.

The increase in near-wall momentum deficit observed in Figure 8 can be directly linked to modifications of the flow topology both inside and above the liner orifices. The presence of the perforated surface enhances streamwise velocity fluctuations in the near-wall region and generates strong wall-normal fluctuations within the orifices. The flow predominantly enters the orifice from its downstream side and impinges on the downstream corner, creating a recirculating structure in the first half as shown by Avallone et al. [21].

At low acoustic forcing (130 dB), these modifications remain relatively weak, and the flow field closely resembles the unforced case, consistent with the modest changes in the mean velocity profiles. In contrast, at high forcing levels (145 dB), a marked amplification of both streamwise and wall-normal fluctuations is observed. This behaviour is associated with periodic ejection and ingestion of fluid through the orifices [36], driven by the acoustic pressure field. These oscillatory motions enhance the exchange of mass and momentum between the cavity and the grazing flow,

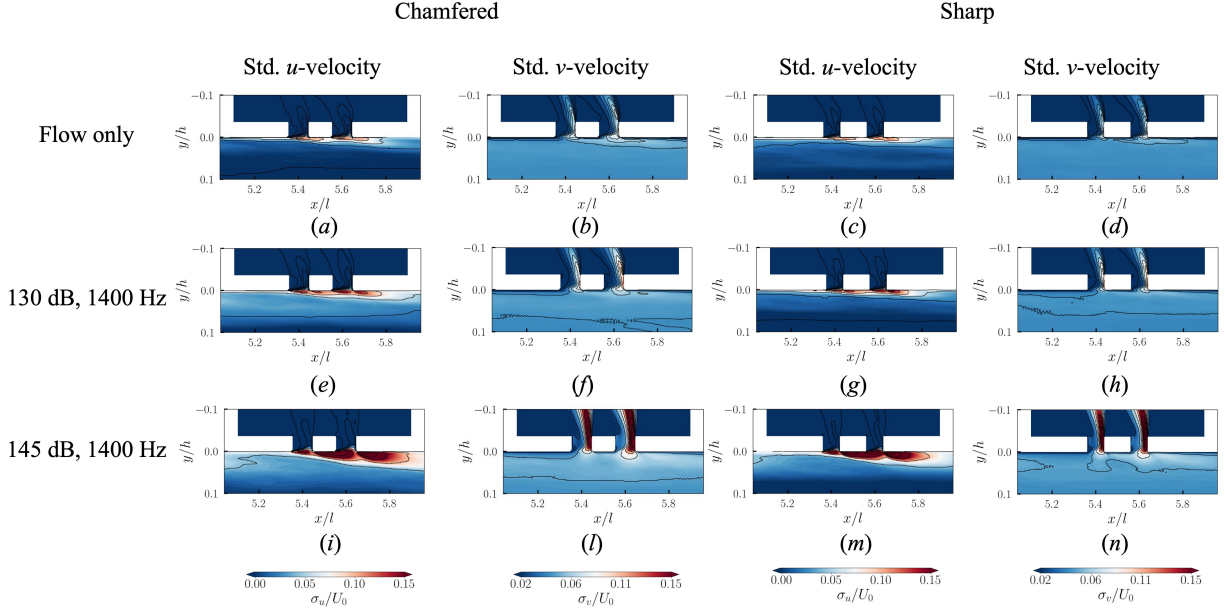


Fig. 10 Contours of the standard deviation of the streamwise (a, c, e, g, i, m) and wall-normal (b, d, f, h, l, n) velocity components over the sixth cavity. Chamfered (a, b, e, f, i, l) and sharp-edged (c, d, g, h, m, n) configurations are compared at different SPLs for $f = 1.4$ kHz and $M = 0.3$.

intensifying the impingement on the downstream corner and strengthening the local shear layer.

The acoustic-induced motion also alters the near-wall flow downstream of the orifice (see Figures 10(g–h)), promoting stronger interaction between the inner and outer regions of the turbulent flow. This results in enhanced turbulent mixing and increased momentum transport away from the wall and increased displacement thickness. Such mechanisms provide a physical explanation for the observed downward shift of the velocity profiles [38].

A clear dependence on orifice geometry is also observed. The chamfered configuration exhibits more intense and spatially extended velocity fluctuations compared to the sharp-edged case. This indicates a more effective coupling between the cavity flow and the outer boundary layer. As a result, the chamfered geometry enhances near-wall mixing and produces a larger momentum deficit, consistent with the trends observed in the mean velocity profiles and boundary-layer development.

Overall, these results highlight that the near-wall flow organisation is strongly controlled by the interaction between acoustic forcing and orifice geometry. The edge shape alters the porosity, which governs the development of the shear layer and the efficiency of flow exchange through the perforations, thereby playing a key role in both the aerodynamic and acoustic behaviour of the liner.

Complementary contours of $v(|dU/dy|)^{1/2}$, displayed in Figure 11, further illustrate the local shear intensity immediately above the first cavity for the cases without acoustic forcing. The sharp-edged geometry produces more elongated shear layers, whereas the chamfered configuration yields weaker, and more confined shear structures. As the flow develops downstream, the shear-layer intensity decreases in both cases, but more rapidly for the chamfered liner.

Figure 11(c) reports the streamwise evolution of the mean shear-layer intensity, computed at $y/h = 0$ for the first and second orifice of each cavity in the flow-only case. Both geometries exhibit a decreasing trend along the liner, with the second orifice consistently showing lower shear intensity than the first. This behaviour can be linked to the flow field organisation shown in Figure 10: the second orifice is exposed to higher streamwise velocity and stronger wall-normal fluctuations, which displace the flow away from the wall and reduce the local velocity gradient, thereby weakening the shear layer. This effect is more pronounced in the chamfered configuration, where enhanced momentum mixing between the cavity and the outer region amplifies these fluctuations.

These differences directly affect the interaction between the grazing flow and the perforated surface. In particular, the stronger shear layers associated with the sharp-edged geometry increase the local blockage effect, limiting the penetration of acoustic-induced flow into the cavity. In contrast, the reduced shear in the chamfered configuration facilitates a more efficient exchange of acoustic-induced mass flow. This result in a different acoustic dissipation mechanism depending

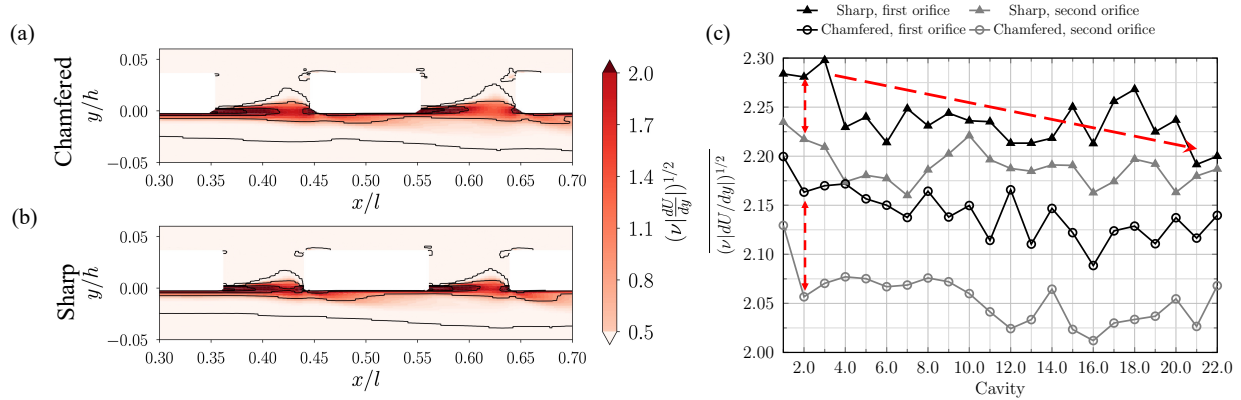


Fig. 11 Shear-layer intensity represented by $\nu(|dU/dy|)^{1/2}$ for the first cavity: (a) chamfered and (b) sharp-edged geometry. (c) Streamwise distribution of the mean shear-layer intensity over the first and second orifice of each cavity for both geometries. Results correspond to the flow-only case with $M = 0.3$.

on the geometry and on the local SPL and shear-layer strength [39]. From a macroscopic perspective, this behaviour can be interpreted as a change in the effective porosity perceived by the grazing flow. Although the internal diameter of the orifices is identical, the chamfered geometry behaves as a more permeable surface, while the sharp-edged configuration acts as a more obstructed one.

V. Conclusion

High-fidelity simulations, supported by experimental comparison, were conducted to investigate the influence of orifice-edge geometry on the acoustic and aerodynamic performance of a perforated liner under turbulent grazing flow. Two configurations were analysed, sharp-edged and chamfered, while keeping all other geometric and flow parameters constant, allowing the isolated effect of edge shape to be assessed.

Across the entire operating range, the sharp-edged liner consistently exhibited up to 50% higher acoustic resistance than its chamfered counterpart, whereas the reactance remained largely unchanged, apart from a shift in resonance frequency from 1.7 kHz to 1.9 kHz. Correspondingly, the chamfered liner provided up to 4 dB higher attenuation near resonance.

The flow-field analysis provides insight into the mechanisms which might underlie these differences. The chamfered geometry acts as a more permeable surface promoting a larger near-wall momentum deficit, a slightly thicker boundary layer displacement thickness, and enhanced interaction between the inner and outer regions of the flow. These features are associated with a weaker and less extended shear layer above the cavities. In contrast, the sharp-edged geometry generates stronger, more extended shear layers and increased flow blockage at the orifice entrance. This difference in flow topology might provide a consistent explanation for the lower resistance and higher acoustic absorption observed in the chamfered configuration.

Overall, the results demonstrate that small geometric variations at the orifice edge, such as those arising from manufacturing tolerances or finishing processes, can significantly alter both the aerodynamic development and the acoustic performance of liners operating under grazing flow.

These insights emphasise the need to account for edge geometry in both liner design and modelling approaches. Future work will focus on quantifying the relationship between local shear-layer characteristics, effective porosity, and acoustic impedance, with the aim of developing predictive models that directly link detailed geometric features to aeroacoustic performance.

VI. Acknowledgments

The authors gratefully acknowledge Lucas Bonomo for sharing the experimental results from his campaign. The work of A. Paduano, F. Scarano and F. Avallone are co-funded by the European Union (ERC, LINING, 101075903). Views and opinions expressed are however those of the author(s) only and do not necessarily reflect those of the European Union or the European Research Council. Neither the European Union nor the granting authority can be

held responsible for them. This work was partially supported by the AeroAcoustics Research Consortium (AARC). The AARC is a government-industry partnership supporting pre-competitive research for aircraft noise reduction. J. A. Cordioli acknowledges funding from the Brazilian funding agency CNPq (National Council for Scientific and Technological Development) through the process 315000/2021-0.

References

- [1] Casalino, D., Hazir, A., and Mann, A., “Turbofan broadband noise prediction using the lattice boltzmann method,” *AIAA Journal*, Vol. 56, No. 2, 2018. <https://doi.org/10.2514/1.J055674>.
- [2] Brown, M. C., Nark, D. M., and Jones, M. G., “Preliminary Design of a Distributed Facesheet Acoustic Liner for Broadband Acoustic Attenuation,” *AIAA Aviation and Aeronautics Forum and Exposition, AIAA AVIATION Forum 2023*, 2023. <https://doi.org/10.2514/6.2023-3638>.
- [3] Panton, R. L., and Miller, J. M., “Resonant frequencies of cylindrical Helmholtz resonators,” *The Journal of the Acoustical Society of America*, Vol. 57, No. 6, 1975, pp. 1533–1535. <https://doi.org/10.1121/1.380596>.
- [4] Melling, T. H., “The acoustic impedance of perforates at medium and high sound pressure levels,” Tech. Rep. 1, 1973.
- [5] Zhang, Q., and Bodony, D. J., “Numerical investigation and modelling of acoustically excited flow through a circular orifice backed by a hexagonal cavity,” *Journal of Fluid Mechanics*, Vol. 693, 2012, pp. 367–401. <https://doi.org/10.1017/jfm.2011.537>.
- [6] Tam, C. K. W., and Kurbatskii, K. A., “Microfluid Dynamics and Acoustics of Resonant Liners,” *AIAA Journal*, Vol. 38, No. 8, 2000, pp. 1331–1339. <https://doi.org/10.2514/2.1132>, URL <https://arc.aiaa.org/doi/10.2514/2.1132>.
- [7] Scarano, F., Paduano, A., and Avallone, F., “Noise dissipation mechanisms of an acoustic liner under grazing flow,” 2025. <https://doi.org/10.48550/arXiv.2512.09587>.
- [8] Jones, M. G., Tracy, M. B., Watson, W. R., and Parrott, T. L., “Effects of liner geometry on acoustic impedance,” *8th AIAA/CEAS Aeroacoustics Conference and Exhibit*, American Institute of Aeronautics and Astronautics Inc., 2002. <https://doi.org/10.2514/6.2002-2446>.
- [9] Gaeta, R. J., and Ahuja, K. K., “Effect of orifice shape on acoustic impedance,” *International Journal of Aeroacoustics*, Vol. 15, No. 4-5, 2016. <https://doi.org/10.1177/1475472X16642133>.
- [10] Zhao, D., Ji, C., and Wang, B., “Geometric shapes effect of in-duct perforated orifices on aeroacoustics damping performances at low Helmholtz and Strouhal number,” *The Journal of the Acoustical Society of America*, Vol. 145, No. 4, 2019. <https://doi.org/10.1121/1.5096642>.
- [11] Cummings, A., “Acoustic nonlinearities and power losses at orifices,” *AIAA Journal*, Vol. 22, No. 6, 1984. <https://doi.org/10.2514/3.8680>.
- [12] Zheng, M., Chen, C., and Li, X., “The influence of the grazing flow and sound incidence direction on the acoustic characteristics of double Helmholtz resonators,” *Applied Acoustics*, Vol. 202, 2023. <https://doi.org/10.1016/j.apacoust.2022.109160>.
- [13] Paduano, A., Scarano, F., Cordioli, J., Casalino, D., and Avallone, F., “On the impact of the turbulent grazing flow development on the acoustic response of an acoustic liner,” *arXiv preprint arXiv:2507.22714*, 2025.
- [14] Avallone, F., Khedr, A., Paduano, A., Scarano, F., Pereira, L., and Cordioli, J., “On the relevance of facesheet orifice geometry to acoustic liner impedance,” *npj Acoustics*, Vol. 2, 2026. <https://doi.org/10.1038/s44384-026-00044-x>.
- [15] Succi, S., *The Lattice Boltzmann Equation for Fluid Dynamics and Beyond*, Oxford University Press, 2001. <https://doi.org/10.1093/oso/9780198503989.001.0001>.
- [16] Qian, Y. H., D’Humières, D., and Lallemand, P., “Lattice bgk models for navier-stokes equation,” *EPL*, Vol. 17, No. 6, 1992. <https://doi.org/10.1209/0295-5075/17/6/001>.
- [17] Yakhot, V., and Orszag, S. A., “Renormalization-group analysis of turbulence,” *Physical Review Letters*, Vol. 57, No. 14, 1986. <https://doi.org/10.1103/PhysRevLett.57.1722>.
- [18] Texeira, C. M., “Incorporating turbulence models into the Lattice-boltzmann method,” *International Journal of Modern Physics C*, Vol. 9, No. 8, 1998. <https://doi.org/10.1142/s0129183198001060>.

- [19] Quintino, N. T., Bonomo, L. A., Cordioli, J. A., Jones, M. G., Howerton, B. M., Nark, D. M., and Avallone, F., “Comparison of Impedance Eduction Test Rigs with Different Boundary-Layer Profiles,” *AIAA Journal*, 2025. <https://doi.org/10.2514/1.J065173>.
- [20] Tam, C. K., Pastouchenko, N. N., Jones, M. G., and Watson, W. R., “Experimental validation of numerical simulations for an acoustic liner in grazing flow: Self-noise and added drag,” *Journal of Sound and Vibration*, Vol. 333, 2014. <https://doi.org/10.1016/j.jsv.2014.02.019>.
- [21] Avallone, F., Manjunath, P., Ragni, D., and Casalino, D., “Lattice-boltzmann very large eddy simulation of a multi-orifice acoustic liner with turbulent grazing flow,” *25th AIAA/CEAS Aeroacoustics Conference, 2019*, 2019. <https://doi.org/10.2514/6.2019-2542>.
- [22] Avallone, F., and Casalino, D., “Acoustic-induced velocity in a multi-orifice acoustic liner grazed by a turbulent boundary layer,” *AIAA Aviation and Aeronautics Forum and Exposition, AIAA AVIATION Forum 2021*, American Institute of Aeronautics and Astronautics Inc, AIAA, 2021. <https://doi.org/10.2514/6.2021-2169>.
- [23] Tam, C. K. W., Ju, H., Jones, M. G., Watson, W. R., and Parrott, T. L., “A computational and experimental study of resonators in three dimensions,” *Journal of Sound and Vibration*, Vol. 329, No. 24, 2010, pp. 5164–5193. <https://doi.org/10.1016/j.jsv.2010.06.005>, URL <https://linkinghub.elsevier.com/retrieve/pii/S0022460X10003779>.
- [24] Elnady, T., and Bodén, H., “An inverse analytical method for extracting liner impedance from pressure measurements,” *Collection of Technical Papers - 10th AIAA/CEAS Aeroacoustics Conference*, Vol. 1, 2004. <https://doi.org/10.2514/6.2004-2836>.
- [25] Elnady, T., Bodén, H., and Elhadidi, B., “Validation of an inverse semi-analytical technique to educe liner impedance,” *AIAA Journal*, Vol. 47, No. 12, 2009. <https://doi.org/10.2514/1.41647>.
- [26] Paduano, A., Scarano, F., Bonomo, L., Casalino, D., Cordioli, J., and Avallone, F., “Influence of Base Flow Modelling and Viscous Effects on Impedance Eduction of Acoustic Liners,” , 01 2026. <https://doi.org/10.2139/ssrn.6505405>.
- [27] Yu, J., Ruiz, M., and Kwan, H. W., “Validation of Goodrich perforate liner impedance model using NASA langley test data,” *14th AIAA/CEAS Aeroacoustics Conference (29th AIAA Aeroacoustics Conference)*, 2008. <https://doi.org/10.2514/6.2008-2930>.
- [28] Levenberg, K., “A method for the solution of certain non-linear problems in least squares,” *Quarterly of Applied Mathematics*, Vol. 2, No. 2, 1944. <https://doi.org/10.1090/qam/10666>.
- [29] Marquardt, D. W., “An Algorithm for Least-Squares Estimation of Nonlinear Parameters,” *Journal of the Society for Industrial and Applied Mathematics*, Vol. 11, No. 2, 1963. <https://doi.org/10.1137/0111030>.
- [30] Dean, P. D., “An in situ method of wall acoustic impedance measurement in flow ducts,” Tech. Rep. 1, 1974.
- [31] Schuster, B., “A comparison of ensemble averaging methods using Dean’s method for in-situ impedance measurements,” *18th AIAA/CEAS Aeroacoustics Conference (33rd AIAA Aeroacoustics Conference)*, 2012. <https://doi.org/10.2514/6.2012-2244>.
- [32] Zhang, Q., and Bodony, D. J., “Numerical investigation of a honeycomb liner grazed by laminar and turbulent boundary layers,” *Journal of Fluid Mechanics*, Vol. 792, 2016, pp. 936–980. <https://doi.org/10.1017/jfm.2016.79>.
- [33] Spillere, A. M. N., Bonomo, L. A., Cordioli, J. A., and Brambley, E. J., “Experimentally testing impedance boundary conditions for acoustic liners with flow: Beyond upstream and downstream,” *Journal of Sound and Vibration*, Vol. 489, 2020. <https://doi.org/10.1016/j.jsv.2020.115676>.
- [34] Bonomo, L. A., Quintino, N. T., Spillere, A. M. N., Cordioli, J. A., and Murray, P. B., “A Comparison of In-Situ and Impedance Eduction Experimental Techniques for Acoustic Liners with Grazing Flow and High SPL,” *28th AIAA/CEAS Aeroacoustics Conference, 2022*, 2022. <https://doi.org/10.2514/6.2022-2998>.
- [35] Shahzad, H., Hickel, S., and Modesti, D., “Permeability and Turbulence Over Perforated Plates,” *Flow, Turbulence and Combustion*, Vol. 109, 2022, pp. 1–14. <https://doi.org/10.1007/s10494-022-00337-7>.
- [36] Scarano, F., Jacob, M. C., and Gowree, E. R., “Drag reduction by means of an array of staggered circular cavities at moderate Reynolds numbers,” *International Journal of Heat and Fluid Flow*, Vol. 102, 2023, p. 109142. <https://doi.org/https://doi.org/10.1016/j.ijheatfluidflow.2023.109142>, URL <https://www.sciencedirect.com/science/article/pii/S0142727X23000413>.
- [37] Scarano, F., Jacob, M. C., and Gowree, E. R., “Large scale structures modification of a spatially evolving turbulent boundary layer grazing over circular cavities,” *International Journal of Heat and Fluid Flow*, Vol. 108, 2024, p. 109486. <https://doi.org/https://doi.org/10.1016/j.ijheatfluidflow.2024.109486>, URL <https://www.sciencedirect.com/science/article/pii/S0142727X2400211X>.

- [38] Chung, D., Hutchins, N., Schultz, M. P., and Flack, K. A., “Predicting the Drag of Rough Surfaces,” *Annual Review of Fluid Mechanics*, Vol. 53, No. Volume 53, 2021, 2021, pp. 439–471. <https://doi.org/https://doi.org/10.1146/annurev-fluid-062520-115127>, URL <https://www.annualreviews.org/content/journals/10.1146/annurev-fluid-062520-115127>.
- [39] Scarano, F., Paduano, A., and Avallone, F., “Noise dissipation mechanisms in a multi-cavity acoustic liner grazed by turbulent flow and acoustic waves,” *32th AIAA/CEAS Aeroacoustics Conference*, American Institute of Aeronautics and Astronautics Inc., 2026.